THE JOURNAL OF PHYSICAL CHEMISTRY Letters

Letter

pubs.acs.org/JPCL

Importance of Ion Packing on the Dynamics of Ionic Liquids during Micropore Charging

Yadong He,[†] Rui Qiao,*[,†] Jenel Vatamanu,[§] Oleg Borodin,[‡] Dmitry Bedrov,[§] Jingsong Huang,[∥] and Bobby G. Sumpter[∥]

[†]Department of Mechanical Engineering, Virginia Tech, Blacksburg, Virginia 24061, United States

[‡]Electrochemistry Branch, U.S. Army Research Laboratory, Adelphi, Maryland 20783, United States

[§]Department of Materials Science & Engineering, University of Utah, Salt Lake City, Utah 84112, United States

[∥]Center for Nanophase Materials Sciences and Computer Science & Mathematics Division, Oak Ridge National Laboratory, Bethel Valley Road, Oak Ridge, Tennessee 37831, United States

Supporting Information

ABSTRACT: Molecular simulations of the diffusion of $EMIM^+$ and $TFSI^-$ ions in slit-shaped micropores under conditions similar to those during charging show that in pores that accommodate only a single layer of ions, ions diffuse increasingly faster as the pore becomes charged (with diffusion coefficients even reaching $\sim 5 \times 10^{-9}$ m^2/s), unless the pore becomes very highly charged. In pores wide enough to fit more than one layer of ions, ion diffusion is slower than in the bulk and changes modestly as the pore becomes charged. Analysis of these results revealed that the fast (or slow) diffusion of ions inside a micropore during charging is correlated most strongly with the dense (or loose) ion packing inside the pore. The molecular details of the ions and the precise width of the pores modify these trends weakly, except when the pore is so narrow that the ion conformation relaxation is strongly constrained by the pore walls.

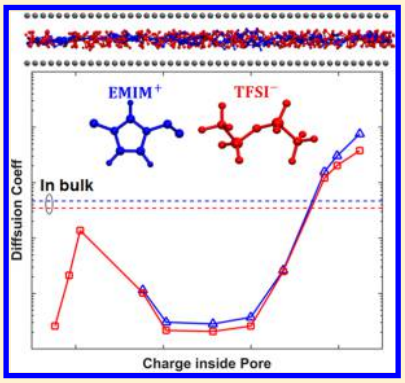

Supercapacitors, also called electrochemical double-layer capacitors (EDLCs), have received significant attention in recent years due to their potential applications in diverse problems such as regenerative braking and grid stabilization.[1−3] By storing electrical energy physically and avoiding time-consuming redox reactions, supercapacitors offer excellent power density and cyclability;[3,4] however, because of their limited energy density, supercapacitors have not been widely deployed until now. Improving the energy density of supercapacitors has been the focus of numerous recent works, and many breakthroughs have been reported.[2,3,5,6] For example, by replacing conventional electrolytes (aqueous electrolytes or organic electrolytes) with room-temperature ionic liquids (RTILs), which have a much wider electrochemical window compared with conventional electrolytes, the energy density of supercapacitors has been improved greatly.[6] Likewise, using porous electrodes with narrow pores helps improve the specific surface area available for energy storage and thus the energy density of supercapacitors.[7] Thanks to the intensive research in recent years, the mechanisms of charge storage in these materials are now reasonably understood.[3,5,8−17] There is, however, a significant concern that the enhanced energy density of supercapacitors achieved using these new materials may come at the cost of reduced power density. In fact, the power density of RTIL-based supercapacitors is often lower compared with those based on aqueous or organic electrolytes (see ref 18 for a review), and this is especially true when RTILs are used together with porous electrodes with mesopores (diameter >2 nm) or micropores (diameter <2 nm) that are the most promising for achieving high energy density. It should be noted that following conventions in the literature, electrodes featuring mesopores or micropores are referred to as nanoporous electrodes because these pores all have diameters on the order of 10^{-9} m. A comprehensive understanding of the origins of the limited power density of current supercapacitors based on RTILs and nanoporous electrodes is lacking. Conceivably, the slow transport of bulky RTIL ions in narrow pores and in bulk electrolytes could lead to sluggish charging/discharging and thus limited power density; however, other factors, for example, ineffective device fabrication and packing, may also be implicated. Because of the limited understanding on this important issue, supercapacitor manufacturers often limit the size of electrode powder to preserve power density, which, in turn, sacrifices the volumetric capacitance and electrical conductance of the electrode. A possible way to improve the rate capability (and thus power density) is to use hierarchical porous electrodes with both micro- and mesopores.[19,20] To facilitate the development of these materials, it is critical to obtain a fundamental understanding of RTILs transport in micro- and mesopores.

Received: October 23, 2015
Accepted: December 7, 2015

DOI: 10.1021/acs.jpclett.5b02378
J. Phys. Chem. Lett. 2016, 7, 36−42

Much of the prior studies of ion transport in nanoporous electrodes focused on the self-diffusion of RTIL ions inside mesopores.[21−25] While the transport of ions in these pores is mostly slower than that in bulk RTILs, the opposite trend has also been observed.[26,27] In comparison, there are fewer studies of ion transport in micropores, and the general expectation is that the diffusion may be slow due to the ultraconfinement; however, in a recent study it was discovered that the highly viscous RTIL 1-ethyl-3-methylimidazolium chloride ([EMIM]-[Cl]) rapidly fills electrically neutral carbon nanotubes as narrow as 1.36 nm, and the ion diffusion inside the idealized nanotube is even faster than that in bulk.[28] Recent studies of the impulsive and cyclic charging of subnanometer pores (diameter <1 nm) with RTILs showed that fast charging (hence high power density) can be achieved in materials with subnanometer pores.[29−31] It was further demonstrated that the fast charging is contributed by the onset of a collective ion transport mode mediated by polarizable pore walls and fast ion diffusion during charging.[29,31] In particular, the self-diffusion coefficient of ions confined in subnanometer pores exhibits a bell-shaped curve as charging proceeds: At the potential of zero charge, ions inside neutral subnanometer pores diffuse very slowly; as charging proceeds, the self-diffusion of ions greatly accelerates, even becoming a few times faster than that in bulk RTILs; their diffusion finally slows down when the pore becomes strongly charged.[29] These results highlight the need to study ion transport under conditions similar to that found during charging of pores. The fact that fast ion dynamics was observed during charging offers hope that one can enhance the energy density of supercapacitors using RTILs and nanoporous electrodes featuring micropores while maintaining satisfactory power density; however, the fast ion dynamics revealed in these studies was obtained using coarse-grained, nearly spherical models of RTILs, in which most atomic details of the ions are neglected. The diffusion of real RTIL ions in micropores, however, is affected by a host of factors including the shape of ions, occupancy of ions inside a pore, binding between specific sites on cations and anions, and steric ion−wall interactions, to name just a few. Obtaining fundamental understanding of the interplay between these factors and electrode potential is a key step toward accelerating the rational design of RTILs for supercapacitors featuring micropores.

In this work, we study the diffusion of 1-ethyl-3-methylimidazolium and bis(trifluoro-methylsulfonyl)-imide ions ($EMIM^+$ and $TFSI^-$) inside slit-shaped micropores using molecular dynamics (MD) simulations with chemically realistic representation of ions using all-atom models (see Figure 1a). The diffusion coefficient of ions inside a pore depends on the internal state of the pore, which can be characterized using the density of cations and anions inside the pore (ρ_+ and ρ_-), or equivalently, the net charge and the total ion density inside the pore ($q = \rho_+ - \rho_-$ and $\rho_\Sigma = \rho_+ + \rho_-$). All densities are presented as area density hereafter because ions form a single layer in most of the pores studied here. When charging a pore, q and ρ_Σ are not uniform along the pore length and vary with time, which makes the quantitative study of ion diffusion under conditions relevant to pore charging complicated; however, prior studies on the impulsive charging of subnanometer pores have shown that the overall charging behavior is closely correlated with the diffusion coefficients of ions inside the pore under quasi-static (infinitely slow) charging conditions.[29] Therefore, once the net charge q inside the pore is known during quasi-static charging, the total ion density inside the pore (ρ_Σ) can be uniquely determined from the thermodynamics of charge storage inside pores, thus making it possible to set up MD simulations to study the ion diffusion. In what follows, we map out the evolution of the self-diffusion coefficients of $EMIM^+$ and $TFSI^-$ ions during the quasi-static charging of several pores. We consider slit pores with center-to-center widths of 0.72, 0.75, and 1.1 nm, in part because the quasi-static charge storage behavior (i.e., ρ_Σ−q relation) in these pores has been previously determined by some of us.[17] The ion compositions in these pores under charging conditions correspond to different potentials on the pore walls and are

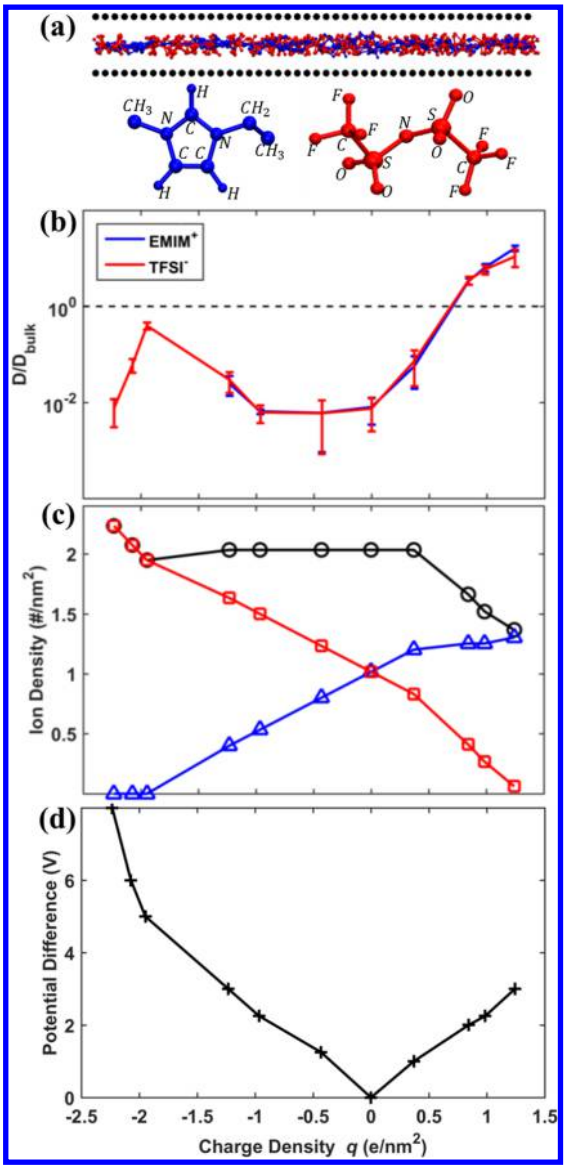

Figure 1. Ion diffusion inside a 0.75 nm slit pore under quasi-static charging conditions. (a) Snapshot of the simulation system and the molecular models of the $EMIM^+$ and $TFSI^-$ ions. (b,c) Scaled ion diffusion coefficient (panel b) and density (panel c) as a function of ionic density q inside the pore during quasi-static charging ($q = \rho_+ - \rho_-$). (d) Potential difference between two nanopores as a function of ionic charge density q. The potential difference is taken as the voltage difference imposed between a pair of pores with the same width and separated by RTIL reservoirs.[17] Panels c and d are adapted from ref 17. The black line in panel c denotes the total ion density. Ion densities in panel c are presented as area density as the ions confined in the pore form a single layer.

DOI: 10.1021/acs.jpclett.5b02378
J. Phys. Chem. Lett. 2016, 7, 36−42

taken from a previous study[17] (also summarized in Tables S1–S3 in the Supporting Information) to set up the diffusion simulations. It is worth noting that, for most charging conditions examined here, there are both cations and anions inside the pores.

First we examined the diffusion of RTIL in a 0.75 nm pore. Figure 1b shows the evolution of the diffusion coefficients of the $EMIM^+$ and $TFSI^-$ ions inside the pore when it is charged under quasi-static conditions. (The applied potential difference corresponding to different charge inside pore is shown in Figure 1d.) The diffusion coefficients of the $EMIM^+$ and $TFSI^-$ ions are close to each other. In addition, they generally increase as charging of the pore proceeds, except when the ionic charge density, q, inside the pore is more negative than -2 e/nm^2. For the $TFSI^-$ ions, the diffusion coefficient approaches their bulk value when q is -2 e/nm^2. On the contrary, the diffusion of $EMIM^+$ ions is faster than in bulk RTIL at $q > 0.7$ e/nm^2 and even becomes faster than Na^+ ions in bulk water for $q \gtrsim 0.9$ e/nm^2.[32] The latter observation is significant because aqueous electrolytes featuring small metal ions are often thought to afford the best power density for supercapacitors due to their high bulk ionic conductivity (or equivalently, the large diffusion coefficient of ions in such electrolytes). Comparison of the ion diffusion coefficients and ion densities inside the pore as a function of pore charge (see Figure 1b, c) indicates that the ion diffusion coefficient inside the pore tends to increase (decrease) as the total ion density ρ_Σ and hence ion packing decreases (increases). These observations are qualitatively similar to that observed from simulations using coarse-grained ions confined in subnanometer pores;[29] however, when the pore becomes more charged while the total ion density inside the pore remains constant, the dependence of the $EMIM^+$ and $TFSI^-$ ion's diffusion coefficients on pore charges is more complicated than that observed with coarse-grained ions. Specifically, for RTILs featuring nearly spherical, coarse-grained ions, the ion diffusion speeds up greatly as the pore becomes charged, even if the total ion density is fixed. This speed-up originates from the fact that as charging proceeds the interlocked cation–anion lattice inside the pore is gradually broken, which facilitates ion diffusion.[29] When the molecular details are included, such a speed-up is indeed observed for the $EMIM^+$ ions when q increases from 0 to ~0.5 e/nm^2 but not for the $TFSI^-$ ions when q decreases from 0 to approximately -1.0 e/nm^2. This asymmetric behavior is likely caused by the fact that $TFSI^-$ ions are slightly more bulky than the $EMIM^+$ ions and they have more tortuous structure with a larger aspect ratio than the disk-like $EMIM^+$ ions, leading to the difference in the efficiency of ion packing inside the pores. Specifically, when charging of the pore proceeds by swapping $EMIM^+$ ions inside the pore with $TFSI^-$ ions in the RTIL reservoir (thus q inside the pore becomes more negative but the total ion density inside pore remains constant),[17,33,34] ions inside the pore become more tightly packed, and the movement of ions becomes more hindered by the irregularly shaped $TFSI^-$ ions.

The critical role of the total ion density (hence ion packing) and the more subtle role of ion shape in determining ion diffusion inside the pore can be rationalized as follows. In the absence of solvents, the movement of a RTIL ion confined in narrow pores is hindered greatly by its neighbors. These neighbors can be thought to form a cage surrounding each ion, and the random diffusion of the ion "locked" in the cage requires the cage to be broken. In a densely populated pore, the breakage of such a cage often must involve coordinated movement of many ions, and hence the ion diffusion is slow. The interlocking of ions with complex shape also compounds the situation, making the diffusion even slower. On the contrary, higher free volume in the less populated cases for $q > 0.7$ e/nm^2 facilitates cage relaxation, making it less susceptible to ion shape, resulting in enhanced ion dynamics for both ions. To corroborate these ideas, we analyzed the breakage of ion cages[35] by computing the time correlation function of ion cages[36]

$$ACF_c(t) = \langle C(0)C(t)\rangle \quad (1)$$

where the bracket $\langle\cdots\rangle$ denotes ensemble average and $C(t)$ is an indicator of the cage around an ion. $C(t)$ is defined as 1.0 if the cage surrounding an ion at $t = 0$ still exists at time t later and zero if the composition of the cage of an ion i at time t is different from that at time $t = 0$ (i.e., the cage is broken). At any given time, to identify which ions form the cage of an ion i, we computed the distance of the ion i to each ion j in the system, $r_{i\text{-}j}$. If $r_{i\text{-}j}$ is smaller than r_{min}, the position of the first valley of the radial distribution function of ion pair i-j in bulk RTILs, then ion j is counted as a member of the cage for ion i. A fast decay of $ACF_c(t)$ toward zero means that the cage surrounding an ion breaks rapidly after forming. Figure 2 shows the $ACF_c(t)$ of

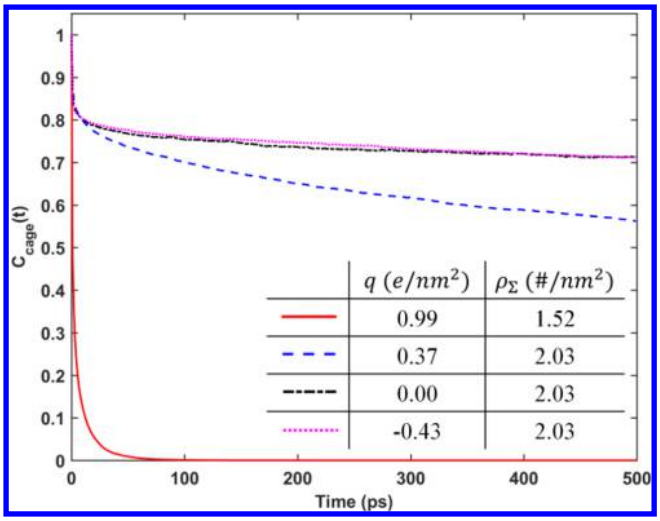

Figure 2. Cage dynamics for $EMIM^+$ ions confined inside a 0.75 nm pore. The dynamics of the "cage" surrounding the $EMIM^+$ ions is characterized using the cage time correlation function (eq 1) in pores with different charge q and total ion density ρ_Σ.

$EMIM^+$ ions confined in the 0.75 nm pore at different levels of charging. (The $ACF_c(t)$ of the $TFSI^-$ ions shows a very similar trend and thus is not shown.) It can be seen that as the total ion density inside the pore ρ_Σ decreases from 2.03 to 1.52 #/nm^2 while the ionic charge inside pore, q, increases from 0.37 to 0.99 e/nm^2, the cage surrounding $EMIM^+$ ions breaks much faster, consistent with the speed-up of $EMIM^+$ ion diffusion shown in Figure 1b. When the pore charge varies from 0 to 0.37 e/nm^2 and from 0 to -0.43 e/nm^2, ρ_Σ is constant. In the former case (q: 0 → 0.37 e/nm^2), the ion cage breaks slightly faster, which is consistent with the moderately faster $EMIM^+$ ion diffusion. The faster cage breakage is due to the presence of more disk-like-shaped $EMIM^+$ ions in the pore, which have less impedance to the breakage of ion cage. On the other hand, in the second case (q: 0 → -0.43 e/nm^2), the dynamics of the cage surrounding $EMIM^+$ ions shows little change, again

DOI: 10.1021/acs.jpclett.5b02378
J. Phys. Chem. Lett. 2016, 7, 36–42

consistent with the fact that the diffusion of $EMIM^+$ ion changes little. This is because more bulky and tortuous $TFSI^-$ ions populate in the pore as the charge decreases from 0, which tends to hinder the breakage of ion cages. The fact that $ACF_c(t)$ decreases notably at short time (t < 30 ps) but decreases very slowly at long time when the pore charge is 0 or −0.43 e/nm^2 indicates that the $EMIM^+$ ions mostly vibrate inside the cage, but the overall motion of all ions is largely arrested. To some extent, $EMIM^+$ ions also diffuse with their "ionic solvation" shell nearly intact, although visualization of ion trajectories suggests that this mode of diffusion does not dominate the ion transport. Overall, the fast (slow) cage dynamics of the $EMIM^+$ ions at short (long) time appears to be consistent with the fact that their mean-square-displacement increases relatively rapidly at short time but very slowly at long time (see Figure S1 in the Supporting Information).

Next, we investigated the diffusion of RTIL in a 0.72 nm pore. The diffusion of the $EMIM^+$ ions in the pore (see Figure 3) shows some features similar to those in the 0.75 nm pores: Their diffusion speeds up as the pore charge increases from 0 to 0.67 e/nm^2, which is accompanied by a decrease in the total ion density inside the pore; their diffusion slows down as the pore charge reduces below zero, when the total ion density inside pore increases. However, the diffusion of $TFSI^-$ ions is quite different from that in the 0.75 nm pore. As can be seen from Figure 3, the diffusion of $TFSI^-$ ions changes little when the pore becomes either positively or negatively charged. The different response of the $EMIM^+$ and $TFSI^-$ ions' diffusion to the charging of the pores originates mostly from the more ellipsoidal shape of the $TFSI^-$ ions compared with the rather planar, disk-like $EMIM^+$ ions. The effect of the difference in shape is especially pronounced when the ions are confined in the narrower 0.72 nm pore. Specifically, because of its ellipsoidal shape, regardless of how a $TFSI^-$ ion is situated within the 0.72 nm pore, its multiple constituent atoms will be in close contact with the pore wall (see Figure 4a). Accordingly, the conformation of the $TFSI^-$ ions is strongly constrained by the pore wall, and the transition between the two different conformers (i.e., C1 and C2 conformers (Figure 4b)) is severely impeded (Figure 4c).

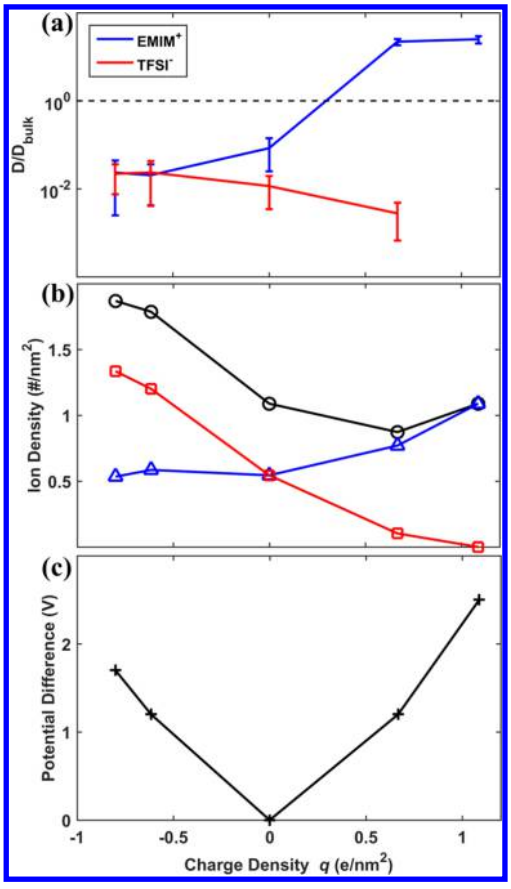

Figure 3. Scaled ion diffusion coefficient (panel a) and density (panel b) as a function of the ionic density q inside a 0.72 nm pore under quasi-static charging conditions. (c) Potential difference between two nanopores as function of ionic charge density q. The potential difference is taken as the voltage difference imposed between a pair of pores with the same width and separated by RTIL reservoirs. Panels b and c are adapted from ref 17. The black line in panel b denotes the total ion density.

Consequently, the steric interactions between the $TFSI^-$ ions and the pore wall dominate the movement of the $TFSI^-$ ions, leading to their inertness in the 0.72 nm pores regardless of the pore charge density. These steric interactions are extremely sensitive to the pore width. In fact, in the 0.75 nm pore, these interactions already become much weaker, as hinted by the more facile transition between their C1 and C2 conformations (see Figure 4c). As a result, the diffusion of $TFSI^-$ ions in the 0.75 nm pore is much faster. For the disk-like $EMIM^+$ ions, which tend to position themselves along the middle plane of the 0.72 nm pore, few of their atoms are in close contact with the wall atoms. Hence, the diffusion of $EMIM^+$ ions is not restricted by the wall but instead governed more strongly by caging from other ions. To ascertain that it is the ion−wall interactions rather than other factors such as ion−ion interactions that dominate the slow diffusion of $TFSI^-$ ions in the 0.72 nm pore, we repeated the simulation with q = 0.67 e/nm^2 and ρ_Σ = 0.87 #/nm^2 by increasing the pore width from 0.72 to 0.75 nm without changing the number of ions inside the pore. The diffusion coefficient of $TFSI^-$ ions was found to increase by ∼100 times, thus confirming the decisive role of steric ion-wall interactions in controlling the diffusion of $TFSI^-$ ions in the 0.72 nm pore.

Finally, we compare the ion packing and dynamics within a 1.1 nm pore with the results for 0.72 and 0.75 nm pores. The 1.1 nm pore was chosen because it is wide enough to accommodate two layers of ions. Figure 5 shows the evolution of ion diffusion coefficients and densities inside the pore during charging under the quasi-static condition. Unlike the observations for the narrower pores shown in Figures 1 and 3, the diffusion coefficients of both $EMIM^+$ and $TFSI^-$ vary rather modestly with the pore charge. This is similar to the situation in the mesopores studied by other research groups[21−25] and also in line with the fact that the total ion density inside the pore varies only marginally as the pore becomes charged. Moreover, in the investigated charge range, both $EMIM^+$ and $TFSI^-$ ions only show much slower dynamics than in bulk.

In summary, a complicated and unexpected picture of ion transport in charged micropores has emerged from MD simulations, where complex-shaped ions were represented using all-atom models. In pores that accommodated only one layer of ions, the diffusion coefficient of an ion increases greatly during charging and exceeds the bulk diffusion values or even diffusion coefficients of small monovalent cations in bulk water. In the wider pores that accommodated more than one layer of

DOI: 10.1021/acs.jpclett.5b02378
J. Phys. Chem. Lett. 2016, 7, 36−42

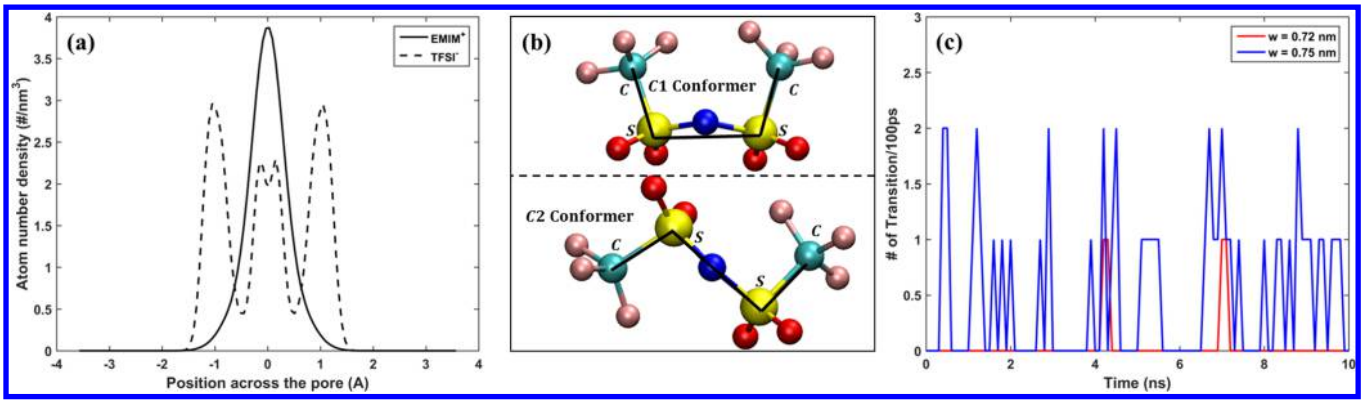

Figure 4. Structures of $EMIM^+$ and $TFSI^-$ ions confined inside micropores. (a) Atom number density profiles of $EMIM^+$ and $TFSI^-$ ions across a 0.72 nm pore (q = 0.67 e/nm^2 and ρ_Σ = 0.87 #/nm^2). Each atom of an ion contributes equally to its atom number density profile. (b) Geometry of the C1 and C2 conformers of a $TFSI^-$ ion. These conformers are distinguished based on the angle of the pseudo-dihedral formed by the C−S−S−C atoms.[37] The yellow, cyan, pink, and red balls denote the S, C, F and O atoms, respectively. (c) Comparison of the rate of transition between the C1 and C2 conformers of $TFSI^-$ ions confined inside the 0.72 nm pore (q = 0.67 e/nm^2, ρ_Σ = 0.87 #/nm^2) and inside the 0.75 nm pore (q = 0.54 e/nm^2, ρ_Σ = 0.88 #/nm^2) during a 10 ns simulation. The transition between the C1 and C2 conformers occurs if the angle of the pseudo-dihedral formed by the C−S−S−C atoms changes by more than 120°.

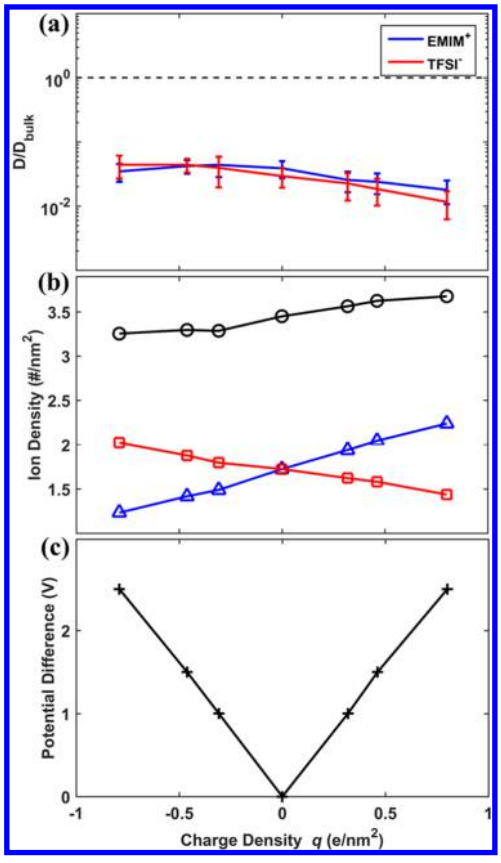

Figure 5. Scaled ion diffusion coefficient (panel a) and density (panel b) as a function of the ionic density q inside a 1.1 nm pore under quasi-static charging conditions. (c) Potential difference between two nanopores as a function of ionic charge density q. The potential difference is taken as the voltage difference imposed between a pair of pores with the same width and separated by RTIL reservoirs. Panels b and c are adapted from ref 17. The black line in panel b denotes the total ion density.

ions, ion diffusion is slower than in bulk RTILs and largely independent of the state of charge. Overall, although many factors affect the ion diffusion, the ion packing typically plays the most important role. These results highlight the importance of understanding the charge dependence of ion diffusion in addition to the pore size dependence. These results also highlight the importance of precisely controlling pore size to realize fast ion diffusion in charged pores. In many practical materials, the large variation of pore size often leads to formation of diffusion bottlenecks as the pore expands and narrows along its length, thus limiting the power density of supercapacitors. Such limitation can potentially be resolved using precisely templated carbons.[38] In the absence of precise pore size control, hierarchical carbons with combined micro- and mesopores may offer the best compromise between energy and power density as large pores will provide the supply of ions to narrow pores with size comparable to the ion sizes.

METHODS

The simulation system consisted of a slab of $EMIM^+$ and $TFSI^-$ ions enclosed between two graphene layers. Three pores with width of 0.72, 0.75, and 1.1 nm were studied. The pore walls measure approximately 6 × 6 nm^2 laterally in all simulations, and periodic boundary conditions were applied in the lateral directions. Inside each pore, for a given net ionic charge, the number of $EMIM^+$ and $TFSI^-$ ions is taken to be the same as that computed in ref 17, which studied the charge storage with the ions considered here in the pores of the same width. The explicit atom (EA)/united atom (UA) models of $EMIM^+$ and $TFSI^-$ ions developed by Vatamanu et al.[39] were adopted for these ions. The carbon atoms in the graphene wall were modeled using the same force fields as in ref 17. The nonelectrostatic, nonbonded interactions in these force fields are a combination of Lennard-Jones (LJ) and Buckingham potential, and the modified Waldman−Hagler combination rules[40] were used to compute the LJ and Buckingham potential parameters for the interaction between two different types of atoms.

Molecular dynamics simulations were performed using the LAMMPS code in the NVT ensemble.[41] The temperature of the ions was maintained at 393 K using a Nosé−Hoover thermostat. The nonelectrostatic interactions were computed via direct summation with a cutoff length of 1.0 nm. The electrical potential on all wall atoms is enforced to be the same, using the LAMMPS subroutine developed in ref 42. Such a

DOI: 10.1021/acs.jpclett.5b02378
J. Phys. Chem. Lett. 2016, 7, 36−42

subroutine computes the electrical charge on the wall atoms at each time step, and thereafter the electrostatic interactions within the system were computed using the P3M (particle-particle particle-mesh) method.[43] The wall atoms were fixed during the simulation. We also performed trial simulations in the 0.75 nm pore in which the wall atoms were allowed to move and their temperature was maintained at 393 K. In those simulations, the intermolecular interactions between the graphene wall's carbon atoms were modeled using the force fields developed by Wei et al.[44] The electrostatic ion−ion interactions were computed based on the electrostatic potential given by[11]

$$\phi(z, R; z_1) = \frac{4}{\epsilon_0 \epsilon_r W} \sum_{n=1}^{\infty} \sin\left(\frac{\pi n z_1}{W}\right) \sin\left(\frac{\pi n z}{W}\right) K_0\left(\frac{\pi n R}{W}\right) \quad (2)$$

where ϵ_0 is the vacuum permittivity, ϵ_r is the dielectric constant (taken as 1.0) in the slit pore, R is the lateral distance between charges, W is the pore width, and $K_0(x)$ is the modified Bessel function of the second kind of order zero. With such an electrostatic potential, the screening of the electrostatic ion−ion interactions by the polarizable pore walls is explicitly considered. While these simulations are significantly more expensive than those previously described, we found that the ion diffusion coefficients obtained in these simulations were very similar to those obtained when the graphene atoms were fixed (see Figure S2 in the Supporting Information). Hence, all results reported in this work were based on the fixed graphene wall simulations.

To generate the initial configuration of the simulation system, we first packed the desired number of ions between the pore walls using the PACKMOL code.[45] After energy minimization, the system was then equilibrated for 10 ns, followed by a production run of 40 ns. A 1 fs time step was used and the trajectories of the ions were saved every 1 ps. The diffusion coefficients of ions were then computed using the Einstein−Helfand method.[46] Specifically, we first compute the mean-square displacement (MSD) of each ion in the xy-plane as a function of time. The MSD is computed for a time T up to 150 ps (when ion diffusion is fast) or 500 ps (when ion diffusion is slow). Such a time is long enough that the MSD increases linearly with time (see Figure S3 in the Supporting Information). Next, we fit the MSD to a linear curve in the time window of 0.6 to 1.0T, and the lateral ion diffusion coefficient is computed as 1/4 of the slope of the fitted linear curve. The latter is consistent with the formula

$$D = \lim_{t\to\infty} (r(t) - r(0))^2/4t \quad (3)$$

where $(r(t) - r(0))^2$ is the ion's mean square displacement in the xy-plane. Sample MSDs for the $TFSI^-$ ions confined in the 0.75 nm pore under various charging conditions are shown in Figure S3 in the Supporting Information. We also computed the MSD in a time window of T = 10 ns for cases in which ions diffuse slowly to assess the diffusion at large time scale. These MSDs exhibit the same trend as revealed by the MSDs in the time window of T = 500 ps, and the diffusion coefficients extracted from these MSDs agree with those extracted from the MSDs in the time window of 500 ps within statistical error (see Figures S4 and S5 in the Supporting Information).

■ ASSOCIATED CONTENT

Supporting Information

The Supporting Information is available free of charge on the ACS Publications website at DOI: 10.1021/acs.jpclett.5b02378.

Equilibrium number densities of $EMIM^+$ and $TFSI^-$ ions inside pores with different widths and potentials (data first reported in ref 17 are adapted and provided for readers' convenience); comparison of the $EMIM^+$ ion's diffusion coefficients computed when pore wall atoms are fixed and are allowed to vibrate; mean square displacement (MSD) of $EMIM^+$ and $TFSI^-$ ions inside 0.75 nm pores; and comparison of the diffusion coefficients computed from MSD with time window of 500 ps and 10 ns. (PDF)

■ AUTHOR INFORMATION

Corresponding Author

*E-mail: ruiqiao@vt.edu.

Notes

The authors declare no competing financial interest.

■ ACKNOWLEDGMENTS

We thank the Clemson-CCIT and ARC at Virginia Tech for generous allocations of computer time on the Palmetto cluster and BlueRidge cluster. R.Q. acknowledges the support from NSF (CBET-1461842). R.Q. was partially supported by an appointment to the HERE program for faculty at the Oak Ridge National Laboratory (ORNL) administered by ORISE. D.B. and J.V. acknowledge the University of Utah MRSEC (NSF grant no. DMR 11-21252) for the support through the seed grant program. J.H. and B.G.S. acknowledge work performed at the Center for Nanophase Materials Sciences, a U.S. DOE Office of Science User Facility.

■ REFERENCES

(1) Gu, W.; Yushin, G. Review of Nanostructured Carbon Materials for Electrochemical Capacitor Applications: Advantages and Limitations of Activated Carbon, Carbide-Derived Carbon, Zeolite-Templated Carbon, Carbon Aerogels, Carbon Nanotubes, Onion-Like Carbon, and Graphene. *Wiley Interdiscip. Rev.: Energy Environ.* **2014**, *3*, 424−473.

(2) *Electrochemical Capacitors: Materials, Systems and Applications*; Béguin, F., Frackowiak, E., Eds.; Wiley-VCH: Weinheim, Germany, 2013.

(3) Simon, P.; Gogotsi, Y. Materials for Electrochemical Capacitors. *Nat. Mater.* **2008**, *7*, 845−854.

(4) Conway, B. E. *Electrochemical Supercapacitors: Scientific Fundamentals and Technological Applications*; Kluwer Academic/Plenum: New York, 1999.

(5) Simon, P.; Gogotsi, Y. Capacitive Energy Storage in Nanostructured Carbon-Electrolyte Systems. *Acc. Chem. Res.* **2013**, *46*, 1094−1103.

(6) Arbizzani, C.; Biso, M.; Cericola, D.; Lazzari, M.; Soavi, F.; Mastragostino, M. Safe, High-Energy Supercapacitors Based on Solvent-Free Ionic Liquid Electrolytes. *J. Power Sources* **2008**, *185*, 1575−1579.

(7) Largeot, C.; Portet, C.; Chmiola, J.; Taberna, P.-L.; Gogotsi, Y.; Simon, P. Relation between the Ion Size and Pore Size for an Electric Double-Layer Capacitor. *J. Am. Chem. Soc.* **2008**, *130*, 2730−2731.

(8) Fedorov, M. V.; Kornyshev, A. A. Ionic Liquids at Electrified Interfaces. *Chem. Rev.* **2014**, *114*, 2978−3036.

(9) Shim, Y.; Kim, H. J. Nanoporous Carbon Supercapacitors in an Ionic Liquid: A Computer Simulation Study. *ACS Nano* **2010**, *4*, 2345−2355.

DOI: 10.1021/acs.jpclett.5b02378
J. Phys. Chem. Lett. 2016, 7, 36−42

(10) Skinner, B.; Chen, T.; Loth, M. S.; Shklovskii, B. I. Theory of Volumetric Capacitance of an Electric Double-Layer Supercapacitor. *Phys. Rev. E* **2011**, *83*, 056102.
(11) Kondrat, S.; Kornyshev, A. Superionic State in Double-Layer Capacitors with Nanoporous Electrodes. *J. Phys.: Condens. Matter* **2011**, *23*, 022201.
(12) Kondrat, S.; Kornyshev, A. Corrigendum: Superionic State in Double-Layer Capacitors with Nanoporous Electrodes. *J. Phys.: Condens. Matter* **2013**, *25*, 119501.
(13) Wu, P.; Huang, J.; Meunier, V.; Sumpter, B. G.; Qiao, R. Complex Capacitance Scaling in Ionic Liquids-Filled Nanopores. *ACS Nano* **2011**, *5*, 9044−9051.
(14) Feng, G.; Cummings, P. T. Supercapacitor Capacitance Exhibits Oscillatory Behavior as a Function of Nanopore Size. *J. Phys. Chem. Lett.* **2011**, *2*, 2859−2864.
(15) Jiang, D.; Jin, Z.; Wu, J. Oscillation of Capacitance inside Nanopores. *Nano Lett.* **2011**, *11*, 5373−5377.
(16) Merlet, C.; Rotenberg, B.; Madden, P. A.; Taberna, P.-L.; Simon, P.; Gogotsi, Y.; Salanne, M. On the Molecular Origin of Supercapacitance in Nanoporous Carbon Electrodes. *Nat. Mater.* **2012**, *11*, 306−310.
(17) Xing, L.; Vatamanu, J.; Borodin, O.; Bedrov, D. On the Atomistic Nature of Capacitance Enhancement Generated by Ionic Liquid Electrolyte Confined in Subnanometer Pores. *J. Phys. Chem. Lett.* **2013**, *4*, 132−140.
(18) Brandt, A.; Pohlmann, S.; Varzi, A.; Balducci, A.; Passerini, S. Ionic Liquids in Supercapacitors. *MRS Bull.* **2013**, *38*, 554−559.
(19) Kajdos, A.; Kvit, A.; Jones, F.; Jagiello, J.; Yushin, G. Tailoring the Pore Alignment for Rapid Ion Transport in Microporous Carbons. *J. Am. Chem. Soc.* **2010**, *132*, 3252−3253.
(20) Rose, M.; Korenblit, Y.; Kockrick, E.; Borchardt, L.; Oschatz, M.; Kaskel, S.; Yushin, G. Hierarchical Micro- and Mesoporous Carbide-Derived Carbon as a High-Performance Electrode Material in Supercapacitors. *Small* **2011**, *7*, 1108−1117.
(21) Monk, J.; Singh, R.; Hung, F. R. Effects of Pore Size and Pore Loading on the Properties of Ionic Liquids Confined Inside Nanoporous CMK-3 Carbon Materials. *J. Phys. Chem. C* **2011**, *115*, 3034−3042.
(22) Rajput, N. N.; Monk, J.; Hung, F. R. Structure and Dynamics of an Ionic Liquid Confined Inside a Charged Slit Graphitic Nanopore. *J. Phys. Chem. C* **2012**, *116*, 14504−14513.
(23) Singh, R.; Rajput, N. N.; He, X.; Monk, J.; Hung, F. R. Molecular Dynamics Simulations of the Ionic Liquid [$EMIM^+$]-[$TFMSI^-$] Confined Inside Rutile (110) Slit Nanopores. *Phys. Chem. Chem. Phys.* **2013**, *15*, 16090−16103.
(24) Rajput, N. N.; Monk, J.; Singh, R.; Hung, F. R. On the Influence of Pore Size and Pore Loading on Structural and Dynamical Heterogeneities of an Ionic Liquid Confined in a Slit Nanopore. *J. Phys. Chem. C* **2012**, *116*, 5169−5181.
(25) Singh, R.; Monk, J.; Hung, F. R. Heterogeneity in the Dynamics of the Ionic Liquid [$BMIM^+$][PF_6^-] Confined in a Slit Nanopore. *J. Phys. Chem. C* **2011**, *115*, 16544−16554.
(26) Shi, W.; Sorescu, D. C. Molecular Simulations of CO_2 and H_2 Sorption into Ionic Liquid 1-n-Hexyl-3-methylimidazolium Bis-(trifluoromethylsulfonyl)amide ([hmim][Tf_2N]) Confined in Carbon Nanotubes. *J. Phys. Chem. B* **2010**, *114*, 15029−15041.
(27) Iacob, C.; Sangoro, J. R.; Kipnusu, W. K.; Valiullin, R.; Kaerger, J.; Kremer, F. Enhanced Charge Transport in Nano-Confined Ionic Liquids. *Soft Matter* **2012**, *8*, 289−293.
(28) Chaban, V. V.; Prezhdo, O. V. Nanoscale Carbon Greatly Enhances Mobility of a Highly Viscous Ionic Liquid. *ACS Nano* **2014**, *8*, 8190−8197.
(29) Kondrat, S.; Wu, P.; Qiao, R.; Kornyshev, A. Accelerating Charging Dynamics in Sub-Nanometer Pores. *Nat. Mater.* **2014**, *13*, 387−393.
(30) Pean, C.; Merlet, C.; Rotenberg, B.; Madden, P. A.; Taberna, P.-L.; Daffos, B.; Salanne, M.; Simon, P. On the Dynamics of Charging in Nanoporous Carbon-Based Supercapacitors. *ACS Nano* **2014**, *8*, 1576−1583.
(31) He, Y.; Huang, J.; Sumpter, B. G.; Kornyshev, A. A.; Qiao, R. Dynamic Charge Storage in Ionic Liquids-Filled Nanopores: Insight from a Computational Cyclic Voltammetry Study. *J. Phys. Chem. Lett.* **2015**, *6*, 22−30.
(32) Fell, C. J. D.; Hutchison, H. P. Diffusion Coefficients for Sodium and Potassium Chlorides in Water at Elevated Temperatures. *J. Chem. Eng. Data* **1971**, *16*, 427−429.
(33) Wu, P.; Huang, J.; Meunier, V.; Sumpter, B. G.; Qiao, R. Voltage Dependent Charge Storage Modes and Capacity in Subnanometer Pores. *J. Phys. Chem. Lett.* **2012**, *3*, 1732−1737.
(34) Bhuiyan, L. B.; Lamperski, S.; Wu, J.; Henderson, D. Monte Carlo Simulation for the Double Layer Structure of an Ionic Liquid Using a Dimer Model: A Comparison with the Density Functional Theory. *J. Phys. Chem. B* **2012**, *116*, 10364−10370.
(35) Schroder, C. Collective Translational Motions and Cage Relaxations in Molecular Ionic Liquids. *J. Chem. Phys.* **2011**, *135*, 024502.
(36) Shi, R.; Wang, Y. Ion-Cage Interpretation for the Structural and Dynamic Changes of Ionic Liquids under an External Electric Field. *J. Phys. Chem. B* **2013**, *117*, 5102−5112.
(37) Fujii, K.; Fujimori, T.; Takamuku, T.; Kanzaki, R.; Umebayashi, Y.; Ishiguro, S. I. Conformational Equilibrium of Bis-(trifluoromethanesulfonyl) Imide Anion of a Room-Temperature Ionic Liquid: Raman Spectroscopic Study and DFT Calculations. *J. Phys. Chem. B* **2006**, *110*, 8179−8183.
(38) Oschatz, M.; Boukhalfa, S.; Nickel, W.; Lee, J. T.; Klosz, S.; Borchardt, L.; Eychmueller, A.; Yushin, G.; Kaskel, S. Kroll-Carbons Based on Silica and Alumina Templates as High-Rate Electrode Materials in Electrochemical Double-Layer Capacitors. *J. Mater. Chem. A* **2014**, *2*, 5131−5139.
(39) Vatamanu, J.; Borodin, O.; Bedrov, D.; Smith, G. D. Molecular Dynamics Simulation Study of the Interfacial Structure and Differential Capacitance of Alkylimidazolium Bis(trifluoromethanesulfonyl)-imide [$C_n$mim][TFSI] Ionic Liquids at Graphite Electrodes. *J. Phys. Chem. C* **2012**, *116*, 7940−7951.
(40) Borodin, O.; Smith, G. D. Development of Many-Body Polarizable Force Fields for Li-Battery Components: 1. Ether, Alkane, and Carbonate-Based Solvents. *J. Phys. Chem. B* **2006**, *110*, 6279−6292.
(41) Plimpton, S. Fast Parallel Algorithms for Short-Range Molecular Dynamics. *J. Comput. Phys.* **1995**, *117*, 1−19.
(42) Wang, Z.; Yang, Y.; Olmsted, D. L.; Asta, M.; Laird, B. B. Evaluation of the Constant Potential Method in Simulating Electric Double-Layer Capacitors. *J. Chem. Phys.* **2014**, *141*, 184102.
(43) Hockney, R. W.; Eastwood, J. W. *Computer Simulation Using Particles*; Adam Hilger: New York, 1989.
(44) Wei, D.; Song, Y.; Wang, F. A Simple Molecular Mechanics Potential for μm Scale Graphene Simulations from the Adaptive Force Matching Method. *J. Chem. Phys.* **2011**, *134*, 184704.
(45) Martinez, L.; Andrade, R.; Birgin, E. G.; Martinez, J. M. PACKMOL: A Package for Building Initial Configurations for Molecular Dynamics Simulations. *J. Comput. Chem.* **2009**, *30*, 2157−2164.
(46) Frenkel, D.; Smit, B. *Understanding Molecular Simulation. From Algorithms to Applications*; Academic Press: San Diego, 1996.

DOI: 10.1021/acs.jpclett.5b02378
J. Phys. Chem. Lett. 2016, 7, 36−42